

RESEARCH LETTER

Open Access



Resonance characteristics and impact of the 2006 Pingtung tsunami in southern Taiwan

An-Chi Cheng^{1,2*} , Anawat Suppasri^{2,3}, Kwanchai Pakoksung³ and Fumihiko Imamura^{2,3}

Abstract

Tsunami resonance excitation induces tsunami amplification, persistent oscillation, and strong current velocities, which may enlarge coastal hazards in tsunamigenic areas. Historically, the 2006 Pingtung earthquake doublet triggered tsunamis that affected the south Taiwan coast. Studying the resonance features based on past tsunamis is important for assessing tsunami hazards and obtaining critical disaster mitigation information. Here, we elucidate the tsunami resonance oscillation and its impacts along the south Taiwan coast based on synthetic assessment of tsunamis induced by the 2006 Pingtung earthquake doublet. A numerical simulation was performed to replicate the 2006 Pingtung earthquake doublet tsunamis. Then, spatially integrated spectra were obtained via spatiotemporal analysis. The results were compared to tsunami spectra at tide gauges to identify the main oscillation modes, suggesting the main oscillation modes had 13–50 min periods during the 2006 Pingtung earthquake doublet tsunamis. The tsunami resonance oscillations were analyzed based on the main oscillation modes. In the 2006 Pingtung earthquake doublet tsunamis, edge waves occurred along the south Taiwan west coast in most oscillation modes. The Hengchun Peninsula prevents tsunami oscillation transmission, and only part of the oscillation energy at certain periods propagates to the east coast. Furthermore, the spectral amplitude distribution migration across the period domain revealed that energy amplification is a frequency-dependent phenomenon and is responsible for the large tsunami heights and strong tsunami-induced current velocities distributed along the south Taiwan coast during this past tsunami.

Introduction

Tsunami resonance is wave fluctuation triggered by multiple wave reflections and the interference of incident tsunamis at the boundary of a bay or continental shelf (Abe 2009; Koshimura 2002; Koshimura et al. 1996). The resonance process is excited when the incident tsunami arrives inside the semi-enclosed basin of a bay

or continental shelf. This coastal process can be strong depending on the tsunami wavelength. It can trigger natural oscillation when the incident tsunami period is consistent with the fundamental modes of the local bathymetry (Loomis 1966; Yamanaka and Nakamura 2020; Koyano et al. 2021; Wang et al. 2021). The excitation of the natural oscillation can cause larger tsunami hazards with higher run-up, amplified tsunami height and persistent tsunami oscillation (Munger and Cheung 2008; Roeber et al. 2010; Yamazaki and Cheung 2011; Melgar and Ruiz-Angulo 2018; Heidarzadeh et al. 2021). In addition, the strong current velocities induced by high-energy tsunamis inside bays or ports can result in severe damage to marine vessels and aquacultural facilities (Suppasri et al. 2014, 2018; Muhari et al. 2015). The coupling of wave shoaling and the resonant response of

*Correspondence:

An-Chi Cheng

cheng.anchi.r6@dc.tohoku.ac.jp

¹ Civil and Environmental Engineering, Graduate School of Engineering, Tohoku University, Sendai, Japan

² WISE Program for Sustainability in the Dynamic Earth, Tohoku University, Sendai, Japan

³ International Research Institute of Disaster Science, Tohoku University, Sendai, Japan

coastal topography to the incident tsunami can increase the level of coastal hazards. For instance, such coupling in Sendai Bay, Japan, was responsible for large tsunami waves with heights of up to 1.5 m following the 2016 Fukushima earthquake, which is unexpected from an M_w 6.9 earthquake (Suppasri et al. 2017; Adriano et al. 2018).

Relevant methods have been developed and applied to analyze tsunami resonance characteristics in tsunamigenic areas worldwide. For example, Yamazaki and Cheung (2011) investigated tsunami trapping and energy amplification over the continental shelf of the 2010 Chile earthquake tsunami. They applied spectral analysis to the synthetic time series computed at all calculated grids from numerical modeling to examine the patterns of large-scale tsunami oscillation and its impacts on the Chilean coast. Aránguiz (2015) found the natural oscillation modes of Concepcion Bay, Chile, using empirical orthogonal function (EOF) analysis. They found that the large tsunami amplification at the south shore of Concepcion Bay, Chile, from the 1960 and 2010 earthquake tsunamis was related to tsunami resonance and coupling between shelf resonance and natural oscillation of the bay. Tanioka et al. (2019) numerically computed the natural oscillation modes inside Hakodate Bay, Japan, by solving the eigenvalues of natural oscillation modes calculated from linear water equations. They found that the large later phases observed in Hakodate Bay, Japan, from the 2011 Tohoku-oki earthquake tsunami were mainly excited by the bay resonance. Heidarzadeh et al. (2021) studied the long period tsunami oscillation (> 20 h) in the basin of the Aegean Sea basin following the recent M_w 7.0 earthquake using spectral analysis. They concluded that the long tsunami duration recorded at several tide gauges can be attributed to basin and subbasin oscillations inside the Aegean Sea. In Taiwan, Cheng et al. (2023) applied wavelet transform analysis to tsunami time series from tide gauge records to investigate the wave trapping of the 2006 Pingtung earthquake doublet. They found that the trapping of incident tsunamis due to the local topography and continental shelf in front of the Hengchun Peninsula are responsible for tsunami amplification and persistent oscillation. Most recently, Heidarzadeh et al. (2022) applied wavelet analysis to DART and tide gauge records and showed that the dominant modes during the January 2022 Tonga tsunami were 4–7 min and 10–17 min, respectively.

Positioned at the convergent boundaries between the Eurasian Plate and Philippine Sea Plate, Taiwan is under the potential threat of earthquake tsunamis. The estimated convergent rate at the boundary region is approximately 80–85 mm yr⁻¹ (Hsu et al. 2009, 2012; Sun et al. 2018); therefore, earthquake activities are frequent both on and offshore Taiwan. The large shallow earthquakes

that occur offshore Taiwan are tsunamigenic, and the most well-known historical earthquake-generated tsunamis that occurred around Taiwan are the 1771 Yaeyama earthquake tsunami (Imamura et al. 2001; Nakamura 2009; Miyazawa et al. 2012; Okinawa Prefectural Government 2015), 1867 Keelung earthquake tsunami (Cheng et al. 2016; Sugawara et al. 2019), and the 2006 Pingtung earthquake doublet tsunami (Wu et al. 2008; Cheng et al. 2023). In previous studies, many attempts have been made to investigate the earthquake source characteristics and generation mechanisms of historical tsunamis. However, the tsunami resonance characteristics and the oscillation patterns along the Taiwan coast, especially in southern Taiwan and the Hengchun Peninsula, have not been well-investigated. It is critical to study the resonance features from past tsunamis, as it is an important step toward understanding tsunami hazards in Taiwan.

In this study, the tsunami wave as well as the resonance characteristics in southern Taiwan were studied, considering the tsunami sources of the 2006 Pingtung earthquake doublet. The structure of this study included the following three aspects: (1) replicate the past tsunamis of the 2006 Pingtung earthquake doublet, (2) perform spatiotemporal analysis on the process time series of the modeled tsunami wavefield and determine the main oscillation modes, and (3) analyze the tsunami oscillation patterns and resonant process with a focus on the main oscillation modes. The present study is the first attempt to investigate the tsunami oscillation patterns and resonance characteristics in southern Taiwan based on the synthetic assessment of modeled earthquake-generated historical tsunamis of the 2006 Pingtung earthquake doublet. The findings of this work, combined with earlier studies, have implications for coastal management and emergency planning to reduce disaster risks from future tsunamis.

Tsunami data

Observed tsunami data

Tide gauge data offer one source of information on tsunami wave patterns by reflecting time series changes in sea levels at coastal sites (Otake et al. 2020). The coastal tide records of the 2006 Pingtung earthquake in southern Taiwan are collected. Recorded data from the three coastal tide gauges are obtained and used for analysis: Dongkung, Houbihu, and Chengkung. The Dongkung tide gauge is located on the west coast. The Houbihu tide gauge is located on the cape of the Hengchun Peninsula. The Chengkung tide gauge is located on the Pacific Ocean side of Taiwan. These tide gauges belong to and are operated by the Central Weather Bureau (CWB), (R.O.C., Republic of China). All tide gauge recorded data have a sampling rate of 6 min. The distribution of the

observation points is plotted in Fig. 1b, and the detailed information is listed in Table 1.

To obtain the tsunami signals, a high-pass filter was applied with a cutoff frequency of 0.000138 Hz (7200 s) to remove the low-frequency tide components from the observed signals (Heidarzadeh and Satake 2013; Ren et al. 2021; Wang et al. 2022a). Based on the study by Heidarzadeh et al. (2015), the bandpass approach is an efficient method that can produce tsunami waveforms that are similar to those removing the calculated tide components from the observed records. The respective earthquake occurrence time (EOT) of the dual earthquakes is 20:26

Table 1 Information on the observation points used for tsunami waveform calculations and Fourier analyses in this study

Tide gauge	Longitude (°E)	Latitude (°N)	Wave gauge	Sea depth (m)
Dongkung	120.43	22.46	Tide gauge	12.0
Houbihu	120.74	21.94	Tide gauge	5.0
Chengkung	121.38	23.09	Tide gauge	8.0

The depth refers to the sea depth at the respective locations in the bathymetry data

(national standard time) and 20:34 (national standard time). Therefore, the time series between 20:00 (national standard time) on 26 December 2006 to 02:00 (national standard time) on 27 December 2006 was chosen for analysis. The observed tsunami signals serve as references to confirm the performance of tsunami simulation.

Synthetic tsunami waveforms

In addition to the observed tsunami data, synthetic tsunamis of two main earthquake sources around the Taiwan region are considered and simulated in this study: the 2006 Pingtung earthquake doublet (M_w 7.0 and M_w 6.9; Wu et al. 2008; Cheng et al. 2023), a successive source off the coast of Pingtung County, Taiwan. The epicenters of the dual earthquakes are shown in Fig. 1a.

The synthetic tsunami waveforms are obtained from the forward tsunami simulations. As the initial condition for forward tsunami simulation, the water level changes, because the instantaneous crustal deformation of fault rupture should be inputted as a tsunami source. For the case of the 2006 Pingtung earthquake doublet, the tsunami sources were modeled based on Cheng et al. (2023). The tsunami source model by Cheng et al. (2023) for the 2006 Pingtung earthquake doublet was inferred by sensitivity analysis based on relevant cases of forward tsunami simulations and tide gauge records. The tsunami source model comprises two single faults with a fault area of 40 km × 20 km and uniform slips of 1.66 m (the first earthquake, M_w 7.0) and 1.17 m (the second earthquake, M_w 6.9). The fault orientation of the first earthquake shows a strike of 319°, dip of 69°, and rake of −102°, and the second earthquake shows a strike of 151°, dip of 48°, and rake of 0°. The central depths of the first and second earthquakes are 20 km and 33 km, respectively. The initial water levels calculated from these tsunami sources were directly inputted into the propagation model to produce the synthetic tsunami waveforms. The fault parameters of each source model for generating tsunamis are summarized in Table 2. The earthquake source models of the two tsunamis are plotted in Fig. 2a.

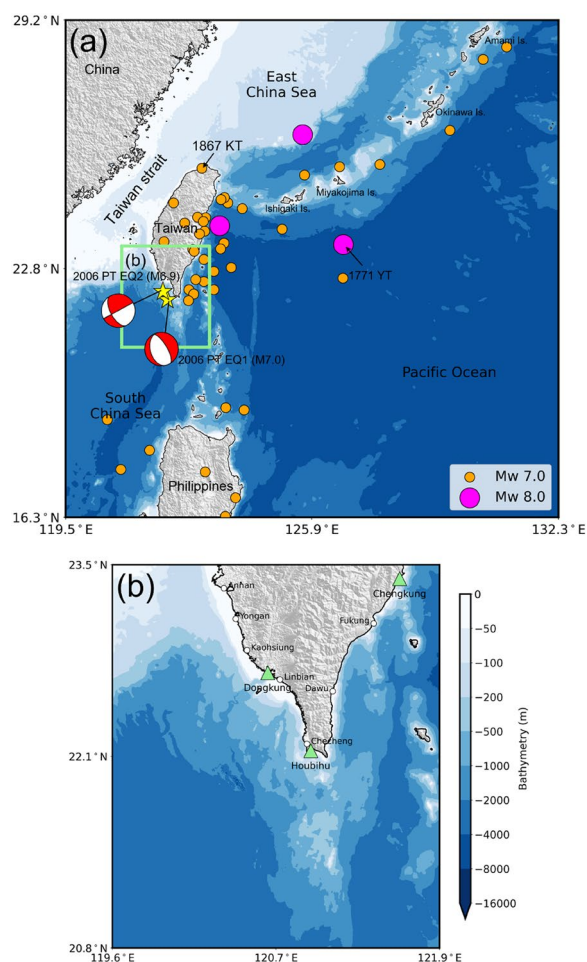


Fig. 1 Bathymetry maps of nested computational domains of **a** grid-1 and **b** grid-2. The green rectangle represents the area of grid-2. Green triangles indicate coastal tide gauges, and white circles indicate the coastal site locations. Orange circles show earthquake events with magnitudes (M_w) > 7.0, and magenta circles illustrate events with magnitudes (M_w) > 8.0. The earthquake information is based on the USGS catalog. Yellow stars represent the locations of earthquake epicenters, and the red beach balls represent the focal mechanisms of the target tsunami events induced by the 2006 Pingtung earthquake doublet

Table 2 Fault parameters for the 2006 Pingtung earthquake doublet to generate tsunamis in this study

Fault parameters for the 2006 Pingtung earthquake doublet		
Reference	Cheng et al. (2023)	
Earthquake	EQ-1	EQ-2
Longitude (°E)	120.55	120.49
Latitude (°N)	21.80	21.97
Length (km)	40	40
Width (km)	20	20
Depth (km)	20	33
Slip (m)	1.66	1.17
Strike (deg)	319	151
Dip (deg)	69	48
Rake (deg)	−102	0
M_w	7.0	6.9

For model validation purposes, the synthetic tsunami waveforms calculated from the tsunami simulation were compared to observed tsunami records at three coastal tide gauges. The locations of the tide gauges operated by the CWB were adopted as our output points for producing synthetic tsunami waveforms.

Bathymetry data

In this study, the bathymetry data of the computational domain for tsunami simulation were created from the 15 arcsec grid resolution of GEBCO-2021. Figure 1 shows the computational domain adopted for the tsunami simulation. To save computational time, two levels of nested grids were employed for the tsunami simulation. The ratio of grid size between the neighboring layers was set to 3:1 to satisfy the requirement of the TUNAMI-N2 package. Grid-1 covers the entire computational area (119.5/132.3/16.3/29.2) with a grid resolution of 450 m. Grid-2 includes all coastal tide stations and synthetic wave gauges in the region of interest (119.6/121.9/20.8/23.5) with a finer bathymetry grid of 150 m. The tsunami signals at coastal sites are strongly affected by the interaction between incoming tsunami waves and the shape of the bordering coastline.

Methods

Numerical tsunami simulation

The purpose of performing a tsunami simulation is to calculate the synthetic waveforms and tsunami wavefield in a spatial domain for waveform and spatiotemporal analysis. For the tsunami simulation, the numerical package TUNAMI-N2 (Tohoku University's Numerical

Analysis Model for Investigation of Nearfield Tsunamis No. 2) was used to numerically compute the tsunami propagation from the source area to the coastal region. The TUNAMI-N2 solves the nonlinear theory of the shallow water equation using a leap-frog scheme on a staggered grid system (Imamura 1996; Goto et al. 1997). The nonlinear theory of the shallow water equation on the Cartesian coordinate system is presented in Eqs. (1)–(3). A finite difference method is employed to solve the nonlinear equations:

$$\frac{\partial \eta}{\partial t} + \frac{\partial M}{\partial x} + \frac{\partial N}{\partial y} = 0 \quad (1)$$

$$\begin{aligned} \frac{\partial M}{\partial t} + \frac{\partial}{\partial x} \left(\frac{M^2}{D} \right) + \frac{\partial}{\partial y} \left(\frac{MN}{D} \right) \\ + gD \frac{\partial \eta}{\partial x} + \frac{gn^2}{D^{7/3}} M \sqrt{M^2 + N^2} = 0 \end{aligned} \quad (2)$$

$$\frac{\partial N}{\partial t} + \frac{\partial}{\partial x} \left(\frac{MN}{D} \right) + \frac{\partial}{\partial y} \left(\frac{N^2}{D} \right) + gD \frac{\partial \eta}{\partial y} + \frac{gn^2}{D^{7/3}} N \sqrt{M^2 + N^2} = 0 \quad (3)$$

where η is the water level, M and N are the discharge fluxes in the x and y directions, respectively, D is the total water depth, g is the gravitational acceleration value 9.8 m s^{-2} , and n is Manning's roughness coefficient. This nonlinear model accounts for the friction at the sea bottom that possesses energy dissipation, which is represented by Manning's roughness coefficient. Manning's roughness coefficient was equivalently set to $0.025 \text{ s m}^{-1/3}$ for the bottom friction at sea or on dry land. The simulation time step for the time domain in the nested grids was set to 0.1 s to satisfy the stability condition in numerical modeling. The tsunami simulation was conducted for an elapsed time of 5 h for the 2006 Pingtung earthquake doublet. The elapsed time windows of 5 h is appropriate for the tsunami durations according to the size of the event. The tsunami inundation calculation was not included in the simulation, as it required high-resolution near-ocean bathymetry and land data; thus, the reflective boundary condition was due to the coastline.

Okada's theory (Okada 1985) was employed to calculate the coseismic vertical seafloor deformation based on the rectangular fault model using the fault parameters of earthquake sources. In addition, the horizontal seafloor deformation acting on bathymetric slopes can strengthen tsunamis; hence, the contribution of horizontal seafloor deformation to tsunami generation was considered following Eq. (4), which were introduced by Tanioka and Satake 1996:

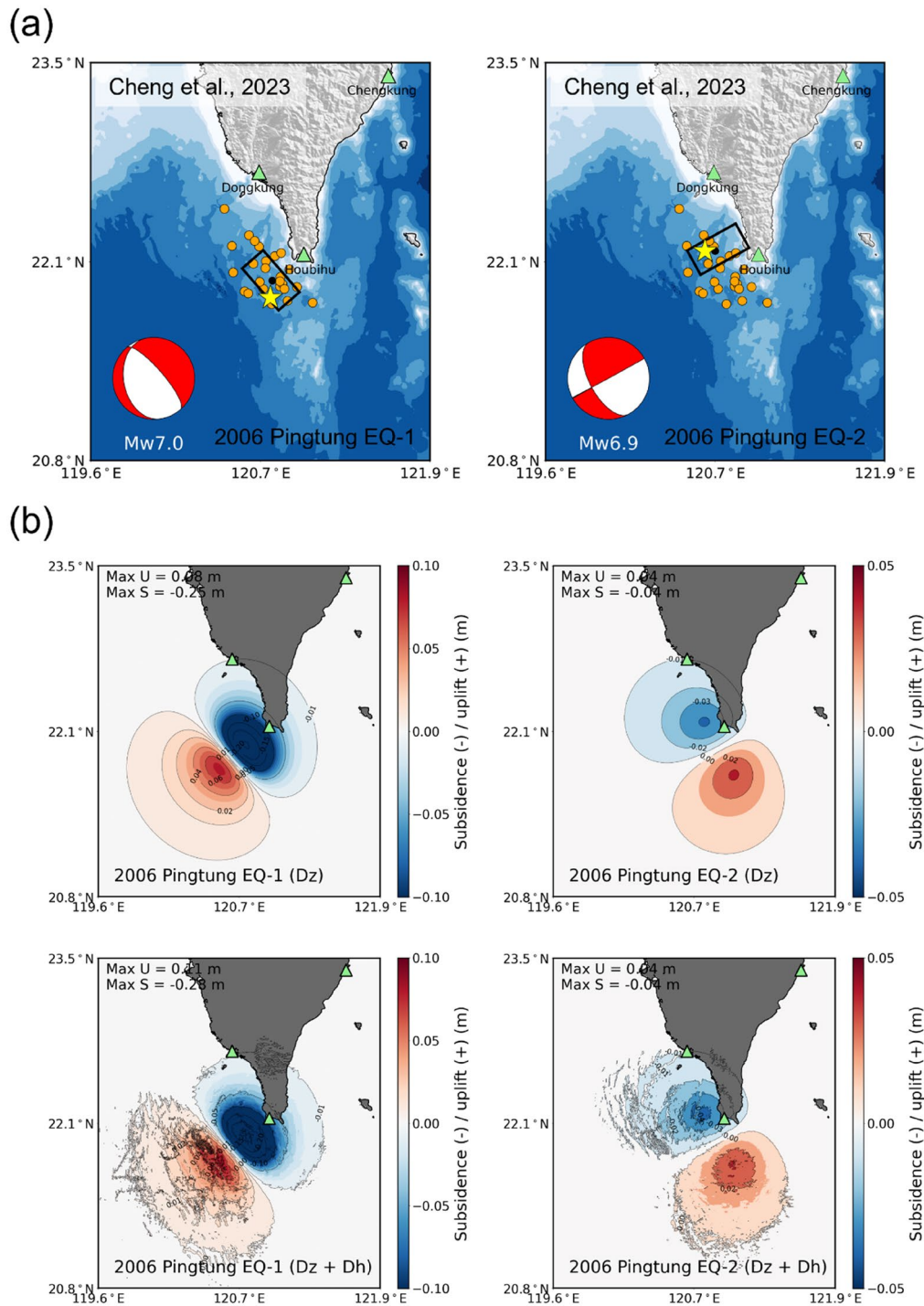


Fig. 2 **a** Tsunami source models of the 2006 Pingtung earthquakes proposed by Cheng et al. (2023). **b** Initial water level change of D_z and $D_z + D_h$ in grid-2 triggered by the 2006 Pingtung earthquakes. Green triangles indicate the tide gauges. Black rectangles illustrate the fault area. Yellow stars represent the locations of earthquake epicenters, and the red beach balls represent the focal mechanisms. Orange circles show the aftershocks that occurred in 1 day. “U” and “S” indicate “uplift” and “subsidence”, respectively

$$D_h = D_x \frac{dH}{dx} + D_y \frac{dH}{dy} \quad (4)$$

where D_x and D_y are the horizontal seafloor deformation in the x and y directions, respectively, H is the water depth (positive downward), D_h is the vertical seafloor deformation contributed by the horizontal seafloor deformation acting on the bathymetric slope, D_z is the vertical seafloor deformation calculated from Okada's theory, and $D_z + D_h$ is the total vertical seafloor deformation. The initial tsunami wavefield is assumed to be the same as the total vertical seafloor deformation and was inputted as the initial condition for propagation computation in the TUNAMI-N2 package. The map of vertical seafloor deformation (D_z) and the total vertical seafloor deformation ($D_z + D_h$) are plotted in Fig. 2b.

Tsunami waveform and Fourier analysis

To evaluate the performance of the numerical tsunami simulation, the synthetic tsunami waveforms obtained from the tsunami simulation are compared to the observed tsunami records at corresponding coastal tide gauges.

After comparing the time series water elevation, the synthetic and observed tsunami waveforms at coastal tide gauges are studied in the frequency domain using Fourier analysis. The Fourier analysis has been widely used in tsunami research and has significantly aided in analyzing tsunami characteristics (Sheehan et al. 2015; Heidarzadeh and Satake 2017; Heidarzadeh et al. 2017; Wang et al. 2022a). The Fourier analysis reveals tsunami oscillation patterns with their frequency characteristics. The Fourier analysis is performed based on the fast Fourier transform (FFT) algorithm using the updated library Numpy, which is included in the Python package (Harris et al. 2020). In this study, Fourier analysis was selected instead of wavelet transform analysis, as it calculates the spectral amplitude and phase angle as a formula of the period, which are essential information to improve the understanding of the oscillation patterns, especially in resonance behavior. Hence, it has been widely applied in tsunami resonance analysis (Roeber et al. 2010; Yamazaki and Cheung 2011).

Fourier analysis is applied to both synthetic and observed tsunami waveforms at each coastal tide gauge to identify the most energetic or predominant periods that may be related to tsunami resonance. The synthetic and observed time series of 5 h were adopted as inputs for Fourier analysis. From the Fourier analysis,

the tsunami spectra illustrate the spectral amplitudes at corresponding periods. The spectral peaks of tsunami spectra show the energetic wave periods at coastal tide gauges during the tsunami. The synthetic spectra are compared to the observed spectra to determine the spectral peaks at coastal tide gauges in each tsunami.

Spatiotemporal analysis

The analysis of tsunami resonance requires identification of the main oscillation modes at coastal tide gauges and their spatial characteristics (Cortés et al. 2017; Ren et al. 2021; Wang et al. 2022b). Thus, Fourier analysis was performed on the process time series of the entire domain of 119.6–121.9°E and 20.8–23.5°N, which is regarded as Grid-2 in our nested computational domain (Fig. 1b). Such spatiotemporal analysis is conducted based on the simulated results, as the analysis requires the migration of entire tsunami wavefields in the time series. The computational domain of Grid-2 covers southern Taiwan and coastal water with a grid resolution of 150 m, which comprises 1612 and 1891 grids in the x and y directions, respectively. In this domain, the simulated tsunami amplitudes at all grids were output as snapshots in minutes and then adopted as inputs for spatiotemporal analysis. Furthermore, the grids of land, rivers, and lakes are excluded using a zero mask according to the GEBCO-2021 topographic data, but no resampling was applied to the simulated tsunami wavefields employed for the spatiotemporal analysis.

The main oscillation modes are determined from the Fourier analysis results of the whole tsunami wavefield and coastal tide gauges. The spatially integrated spectrum is estimated to approach the most compatible modes, and it can be obtained from Eq. (5), which was introduced by Catalán et al. 2015:

$$\hat{S}(p) = \frac{\iint S(x, y, p) dx dy}{\iint dx dy} \quad (5)$$

where $S(x, y, p)$ is the spectrum calculated at each grid, and $\hat{S}(p)$ represents the mean value of the spatially integrated spectrum corresponding to period p . The spatially integrated spectra for both the 2006 Pingtung earthquake doublet is computed and compared with the energetic periods of spectral peaks obtained at the coastal tide gauges to identify the main modes of tsunami oscillation that may be related to the resonant process. The spatial distribution of $S(x, y, p)$ and corresponding phase angles of the identified oscillation modes of the two tsunamis are shown, as described in “Spatiotemporal analysis” section.

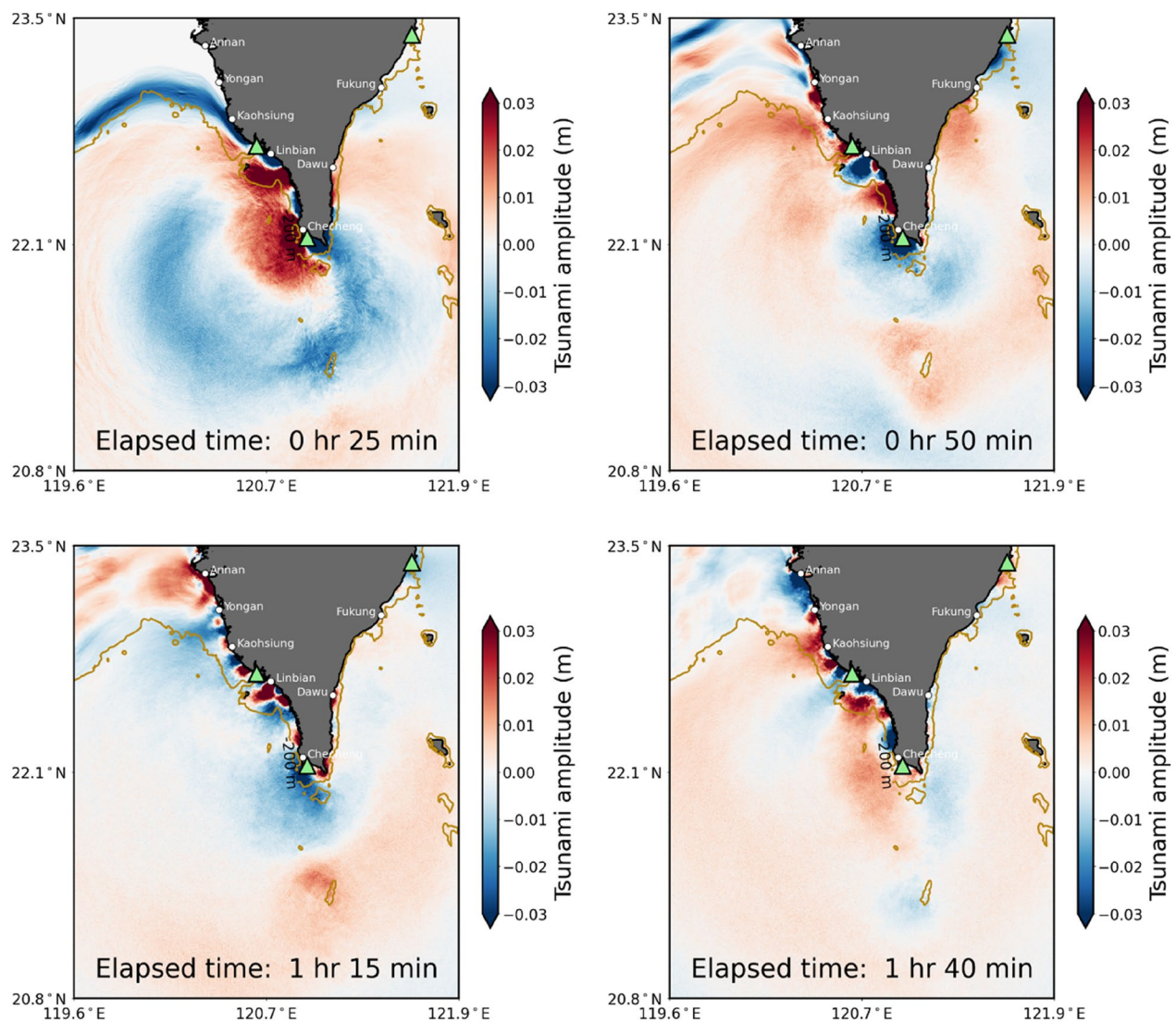


Fig. 3 Snapshots of simulated tsunami propagation in southern Taiwan induced by the 2006 Pingtung earthquakes. Green triangles represent tide gauges. White circles indicate the coastal site locations. The 200 m depth contour is represented by a dark yellow line

Simulated tsunami wavefield and waveform analysis

Simulated tsunami wavefield

The simulated snapshots of tsunami propagation for the 2006 Pingtung earthquake are shown in Fig. 3. The tsunami propagates toward the west coast of Taiwan after it is generated offshore of southern Taiwan, and only a small portion of the tsunami wave diffracts over the peninsula to the east coast. This process is natural, as the continental shelf that extends in front of the west coast has shallower depths compared to the east coast. The tsunami wave is reflected from the shoreline and transmitted toward the Taiwan Strait at a slower speed with shorter wavelengths after arriving at the Houbihu and

Dongkung tide gauges, while part of the tsunami wave is trapped over the continental shelf and propagated along the southwest coast as an edge wave. The southwest coast is a very shallow and wide embayment. According to this coastal feature, the edge wave amplified due to wave shoaling and refracted inside the embayment. The tsunami wave was amplified due to the superposition of the incoming incident and edge wave. Moreover, another explanation for the amplified tsunami along the southwest coast might be attributed to the excitation of natural oscillation due to shelf resonance. The tsunami oscillation along the west coast lasts for several hours after its generation and is gradually weakened because of the absorption and the effect of bottom friction among the

continental shelves; hence, a simulated tsunami wavefield total elapsed time of 5 h following the earthquake occurrence was adopted for analyzing the tsunami resonance of the 2006 Pingtung earthquakes.

The large tsunami heights and the strong tsunami-induced current velocity are important consequences associated with the resonance behaviors (Borrero et al. 2015). To shed light on the tsunami resonance characteristics in southern Taiwan, the simulated maximum tsunami height and maximum current velocity maps are plotted in Fig. 8b, c, respectively. The tsunami energy is released off the coast of southwest Taiwan, which occupies most regions along the west coast. The

large waves and current velocities are concentrated along the west coast, especially at the Dongkung tide gauge and the Linbian, Checheng, and Houbihu tide gauges. The apparent tsunami energy measured along the west coast could be attributed to wave refraction, which transmits the energy of the incident tsunami.

Time series

Figure 4a shows the synthetic and observed tsunami waveforms at three coastal tide gauges from the 2006 Pingtung earthquake doublet. The leading waves of all observed tsunami waveforms are troughs, but the maximum crest amplitudes vary by coastal gauges. For

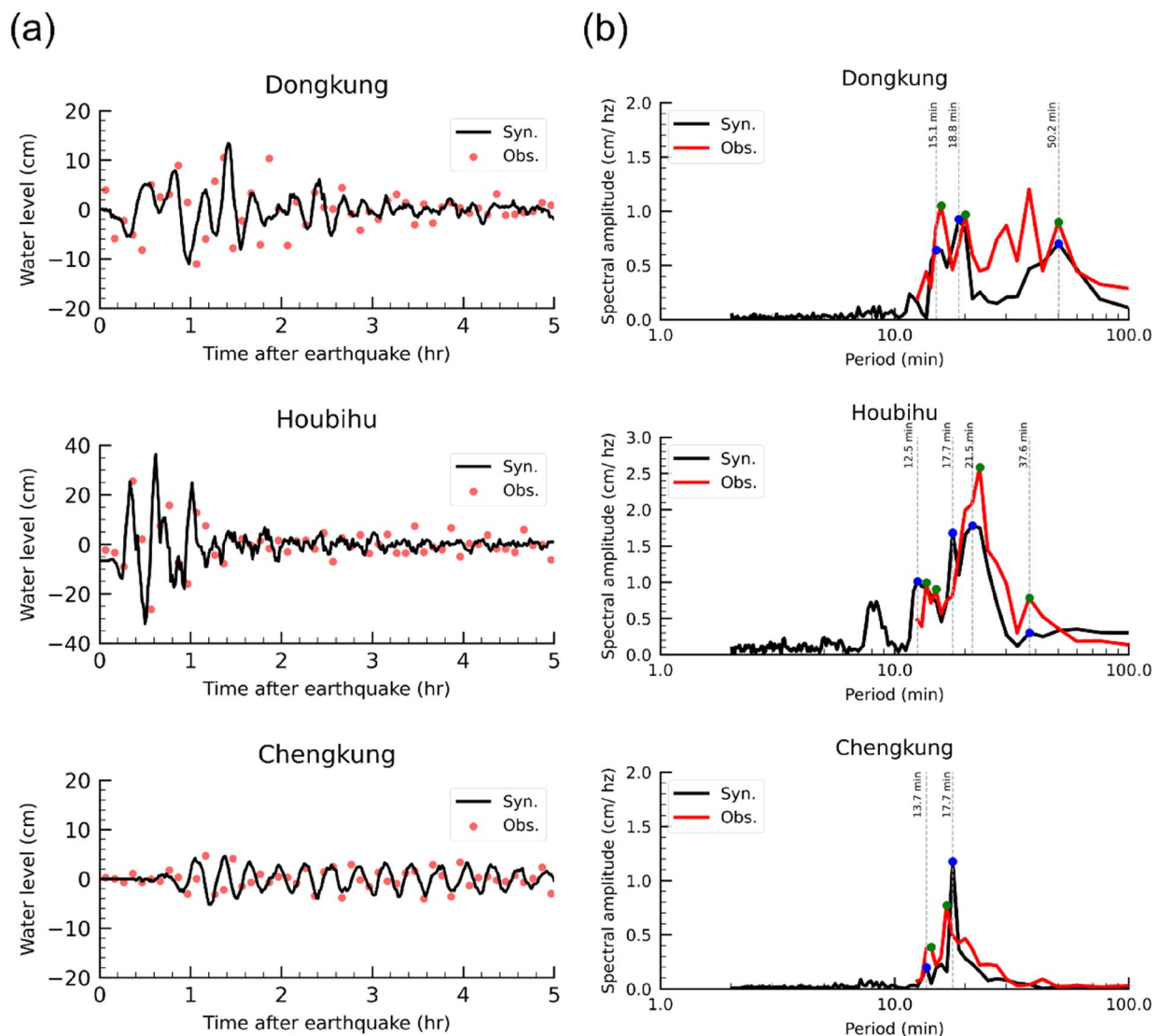


Fig. 4 Synthetic and observed **a** tsunami waveforms and **b** tsunami spectra of the 2006 Pingtung tsunami. The blue and green circles show the comparison of synthetic energetic periods with observed values. The peak periods on the spectra are marked with a gray dashed line

example, the largest crest amplitude at the Houbihu tide gauge exceeds 25 cm, because it is located near the tsunami source region, while the maximum value of 5–10 cm was measured at the Chengkung and Dongkung tide gauges. Another characteristic of the observed and synthetic tsunami waveforms was that the largest wave mostly did not show the first and persistent oscillation in the later phase, which reveals the effect of the resonance process in the bay or continental shelf, where the coastal tide gauge is located.

The arrival times of the synthetic waveforms all agree with those of the observed records of the 2006 Pingtung earthquake tsunami at all three coastal tide gauges. The tsunami amplitudes of the synthetic waveforms were also well-reproduced, including the first wave and later phases, at the Dongkung and Chengkung tide gauges. However, the synthetic waveform at the Houbihu tide gauge was well-replicated in the first crest but slightly underestimated in the second and third wave crests. The discrepancy can be primarily attributed to the bathymetry grids employed for the tsunami simulation. In this study, the finest grid resolution of 150 m for Grid-2 was adopted due to the lack of detailed bathymetric data for accurate simulation of the areas around the coastal tide gauges. Nevertheless, the tsunami simulation still presented satisfactory performances in reproducing the tsunami behaviors in both time series and spectral properties (Fig. 4).

To quantitatively measure the numerical performance, the criterion introduced by Aida (1978) was employed to calculate the forecast accuracy of the tsunami simulation. This criterion has been applied to evaluate the quality-of-match between numerical results and observed records to ensure the reproducibility of the tsunami wave source and propagation model, which is a common procedure (Otake et al. 2020; Heidarzadeh and Mulia 2021; Wang et al. 2022b). The geometric mean ratio (K) of the synthetic (H_s) and observed (H_o) amplitudes are calculated from Eq. (6), and the forecast accuracy can be obtained using Eq. (7):

$$\log(K) = \frac{1}{N} \sum \log \frac{H_o}{H_s} \quad (6)$$

$$\frac{1}{K} \times 100\%(K \geq 1) \quad \text{or} \quad K \times 100\%(K < 1) \quad (7)$$

where N is the total number of coastal tide gauges. The calculated geometric mean ratio (K) and forecast accuracy are summarized in Table 3. Considering the tsunami waveforms at all three coastal tide gauges, the geometric mean ratio (K) is calculated as 1.04 and 0.86 for the synthetic first wave and maximum wave heights, respectively, where the forecast accuracy can be derived

Table 3 Validation of synthetic waveforms at tide gauges from the 2006 Pingtung earthquake tsunami based on criterion of Aida, (1978)

	First wave	Maximum wave
Geometric mean ratio (K)	1.04	0.86
Accuracy (%)	96.01	85.52

as 96.01% and 85.52%, respectively. These results reveal that it is appropriate to use the source model of Cheng et al. 2023 as the wave source to simulate the tsunami wavefields of the 2006 Pingtung earthquake with the TUNAMI-N2 package.

Fourier analysis

Figure 4b shows the results of the Fourier analyses for the synthetic and observed tsunami waveforms of two tsunami events at three coastal tide gauges, which are represented as tsunami spectra. The tsunami spectra describe the spectral patterns that were mainly affected by the tsunami source, propagation path, and local bathymetry. According to previous research, the resonant process can be excited by either the tsunami source or the local bathymetry effects (Yamazaki and Cheung 2011; Cortés et al. 2017). In this study, tsunami simulation is used for the spatiotemporal analysis to study the resonance characteristics based on their spectral patterns in a spatial domain. Therefore, it is important to compare the spectra of synthetic and observed tsunami signals in addition to the time series to confirm the quality of tsunami simulation to study the spectral characteristics of tsunami behaviors.

In the spectral domain, the spectral amplitude of synthetic tsunami spectra is generally consistent with those of the observed records of the 2006 Pingtung earthquakes at three coastal tide gauges with similar shapes and energetic peaks. To quantitatively evaluate the quality of the match, the discrepancy percentage (D) between the most energetic periods of synthetic (P_s) and observed (P_o) tsunami waveforms can be evaluated using Eq. (8):

$$D(\%) = \frac{P_s - P_o}{P_o} \quad (8)$$

The energetic peak periods of synthetic and observed tsunami signals at three coastal tide gauges and their discrepancy percentages are summarized in Table 4. Considering the criterion suggested by Cortés et al. (2017) and Wang et al. (2021), the numerical results are compatible when the period discrepancy of the energetic peaks is less than 10%. The period discrepancy can be attributed to the resolution of the nearshore bathymetric

Table 4 Validation of synthetic energetic periods at tide gauges from the 2006 Pingtung earthquake tsunami

Tide gauge	Dongkung			Houbihu			Chengkung		
Data	Syn.	Obs.	Discr. (%)	Syn.	Obs.	Discr. (%)	Syn.	Obs.	Discr. (%)
Periods (min)	50.2	50.2	0	37.6	37.6	0	17.7	16.7	6
	18.8	20.1	−6	21.5	23.2	−7	13.7	14.3	−4
	15.1	15.8	−4	17.7	15.1	17			
				12.5	13.7	−9			

The values were calculated from Fourier analyses. The energetic periods of the observed and synthetic waveforms are shown in green and blue circles in Fig. 4

grids used for the tsunami simulation, where the coastal structures are not included due to the lack of grid resolution (Ren et al. 2021). The calculated energetic peak periods from the tsunami simulation are mostly located in the reasonable domain; however, the period discrepancy between synthetic and observed signals of 17.7 and 15.1 min at Houbihu is slightly larger than 10%. In this sense, the numerical results present a satisfactory performance in reproducing the tsunami spectra, and it is reasonable to use the simulation results for the Fourier analysis in a spatial domain. The simulated energetic peak periods serve as a reference to identify the main oscillation modes of the two tsunami events for tsunami resonance analysis.

Spatiotemporal analysis

Identification of the main oscillation modes

To analyze the resonance characteristics due to tsunamis caused by the 2006 Pingtung earthquake doublet in southern Taiwan, the main oscillation modes are identified from the comparison of spatially integrated spectra of the entire domain of Grid-2 and the energetic peak

periods at individual stations. A similar approach has been applied in previous studies by Catalán et al. (2015) and Wang et al. (2022a, b) to identify the resonant modes of the 2004 Pisagua and 2021 Alaska earthquake tsunamis. In Fig. 5, black curves illustrate the spatially integrated spectra calculated from the Fourier analysis results of all computational grids, and the symbols represent the calculated tsunami spectra at each coastal tide gauge in each tsunami scenario.

Based on the results of Fourier analysis, six main oscillation modes of 50 min, 38 min, 20 min, 18 min, 15 min, and 13 min were identified for the 2006 Pingtung earthquake doublet, as the spatially integrated spectra and stationary spectra both show evident peaks in these periods.

According to Cheng et al. (2023), the tsunami source spectrum of the 2006 Pingtung earthquake doublet was identified in the range of 13.6–23.1 min with the source dimensions varied from 20 to 40 km around the seafloor depth of approximately 300 m. It is noted that the tsunami source spectrum occurs over a period band rather than a single period because of the

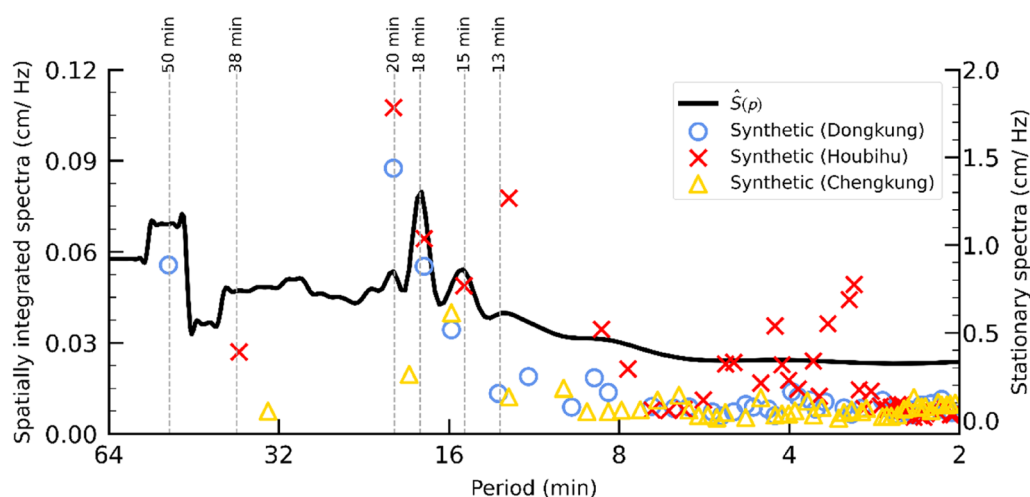


Fig. 5 Comparison of spatially integrated spectra (black solid line) and the stationary spectra (colorful symbols) of the 2006 Pingtung tsunami. The identified main oscillation modes for the respective tsunamis are marked with gray dashed lines

non-uniform shape and non-instantaneous rupture of coseismic crustal deformation. Moreover, according to Abe (2009), the natural periods in the semi-enveloped basins of the bays or continental shelf can be calculated using Merian's equation, as shown in Eq. (9):

$$T_n = \frac{4L}{(2n+1)\sqrt{gh}} \quad (9)$$

where T_n is the natural period of the bay or shelf, L is the dimension measured in the direction perpendicular to the entrance of the bay or shelf, h is the water depth of the bay or shelf, and $n=0, 1, 2, \dots$, which provides various fundamental modes. The coast around southwest Taiwan extends with a constant slope for around 20 km, and the sea depth at the edge of the shelf is around 250 m. From the bathymetry data of GEBCO, the mean sea depth of the shelf is estimated to be 75–125 m. The natural period ($n=0$) of the shelf was calculated to be 38.1–49.1 min. Therefore, the main oscillation periods of 13 min, 15 min, 18 min and 20 min were strongly affected by the tsunami source periods, whereas the local bathymetry, such as shelf features, played a key role in other oscillation periods.

The identified oscillation modes of the respective tsunamis are employed for tsunami resonance analysis based on the spatial distribution of the spectral amplitudes and the phase angles, as presented in “[Resonance impacts](#)” section.

Resonance impacts

Figures 6 and 7 show the spatial distribution of the spectral amplitudes and the phase angles, respectively, of the identified oscillation modes for southern Taiwan with periods of 13–50 min during the 2006 Pingtung earthquake doublet. The spectral amplitude and phase angles were calculated from the Fourier analysis of the simulated time series of each grid. The tsunami oscillation at 50 min illustrates a high energy tsunami wave system, with an antinode appearing over the shelf along the west coast (Figs. 6a, 7a). The antinode contains high tsunami energy, which matched the energetic peaks of 50.2 min on the spectrum at the Dongkung tide gauge (Fig. 4b). This also triggered significant energy amplification in regions around Annan, Yongan, Kaohsiung, and Linbian. The oscillation mode at 38 min presents a similar structure of the wave system but with high energy levels migrating southward (Figs. 6b, 7b). The spectrum of the Houbihu tide gauge included a spectral peak at 37.6 min, which is close to this value (Fig. 4b). As the period decreased from 38 to 20 min, the high energy wave system was shortened as some new nodes appeared along the west coast (Fig. 7c). The oscillation mode at 20 min had energy

amplification mainly concentrated in the regions around Kaohsiung, Linbian, Checheng and Houbihu tide gauges (Fig. 6c). This period was close to the spectral peak of the Houbihu tide gauge at 21.5 min (Fig. 4b). The oscillation mode at 18 min presents a high-energy wave with antinodes that are mainly distributed inside the embayment between the Dongkung and Houbihu tide gauges, while a small part of the tsunami energy propagates over the Hengchun Peninsula and is transmitted to the east coast (Figs. 6d, 7d). This period was close to the spectral peaks of the Dongkung tide gauge at 18.8 min, the Houbihu tide gauge at 17.7 min, and the Chengkung tide gauge at 17.7 min (Fig. 4b). Similarly, the oscillation mode at 15 min shows antinodes with apparent energy amplification over the shelf along the coast of southwest Taiwan (Figs. 6e, 7e). This finding was consistent with the spectral peaks of the Dongkung tide gauge at 15.1 min (Fig. 4b). Unlike other modes, the oscillation period at 13 min presented relatively weak tsunami energy, with the high energy wave system appearing only around the Checheng and Houbihu tide gauges (Figs. 6f, 7f). In addition, at relatively shorter oscillation modes of 18 min, 15 min, and 13 min, an apparent high energy wave existed off the west coast in the Taiwan strait, where the phase angles changed continually. This finding indicates a mechanism of wave diffraction due to the shoaling effect during the passage of the 2006 Pingtung earthquake tsunami. Furthermore, the phase angle migrated rapidly as the period decreased, because tsunami waves with a larger wavelength can be transmitted in a smoother state (Ren et al. 2022).

The tsunami wave patterns of the main oscillation modes reveal that the high energy tsunami waves mainly occurred along the west coast of southern Taiwan during the 2006 Pingtung tsunami. The Hengchun Peninsula hinders transmission of the high-energy tsunami oscillation, and only some tsunami energy at certain periods can pass the obstacle to the east coast. To shed further light on the resonance characteristics of the 2006 tsunami in southern Taiwan, the maximum spectral amplitudes are calculated and plotted, as shown in Fig. 8a. Resonance amplification is concentrated along the west coast of Taiwan, which is similar to the maximum tsunami heights and current velocities simulated along the west coast (Fig. 8b, c). The tsunami reached the west coast from the southwestern direction after generation and was trapped directly over the continental shelf, resulting in resonant oscillation.

Conclusions

Tsunami resonance is a coastal behavior that may enhance coastal hazards with amplified tsunami heights and persistent oscillations in tsunamigenic areas, such

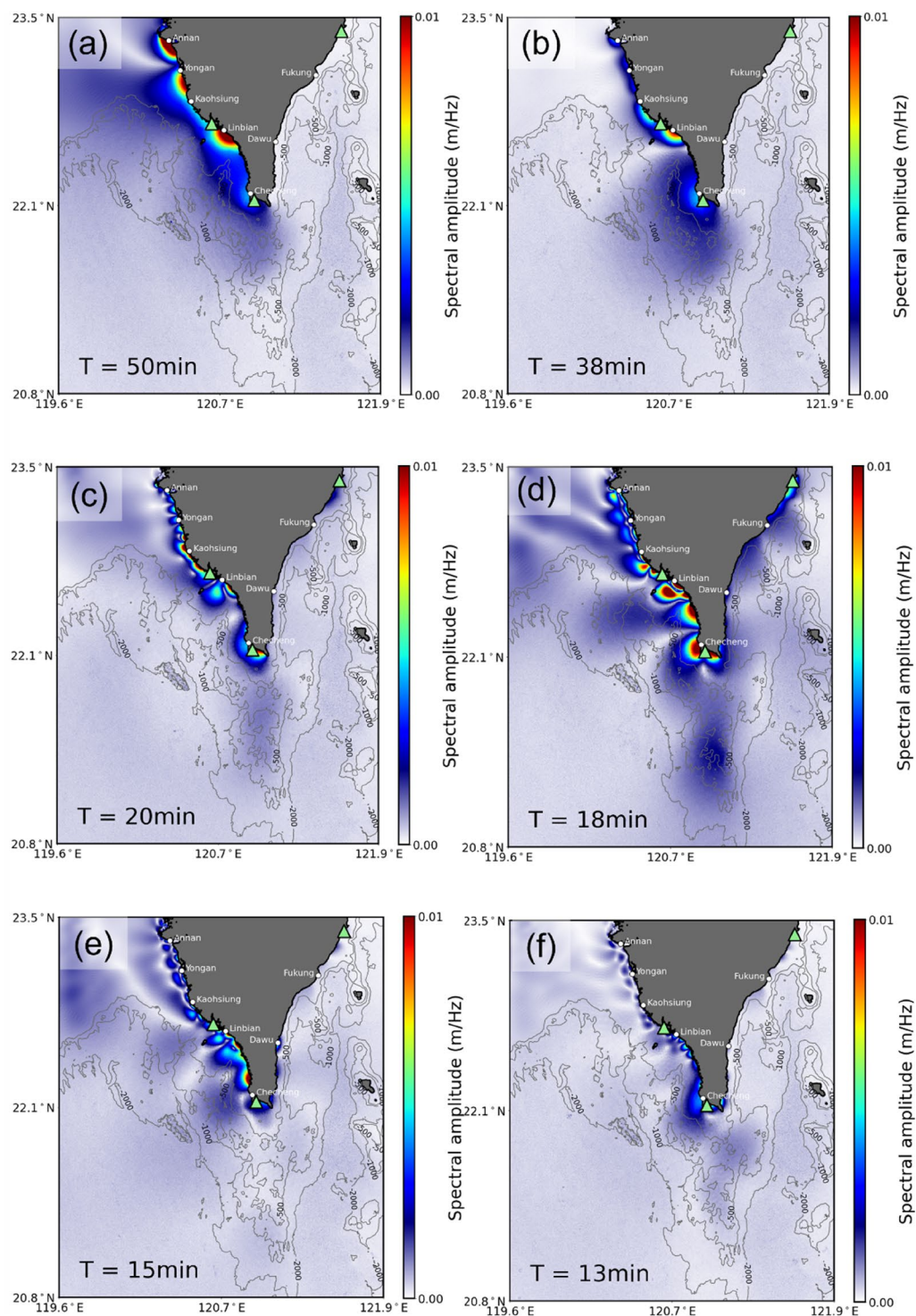


Fig. 6 Spectral amplitudes of resonant oscillation modes in the region of interest (grid-2) from the 2006 Pingtung earthquakes. Green triangles represent tide gauges. White circles indicate the coastal site locations. The bathymetry contours are represented by black solid lines

as southern Taiwan. In this study, numerical tsunami simulation and spatiotemporal analysis are applied to provide a better understanding of tsunami resonance

and its oscillation patterns in southern Taiwan. The simulated tsunami, which was triggered by the modeled earthquake source of the 2006 Pingtung earthquake

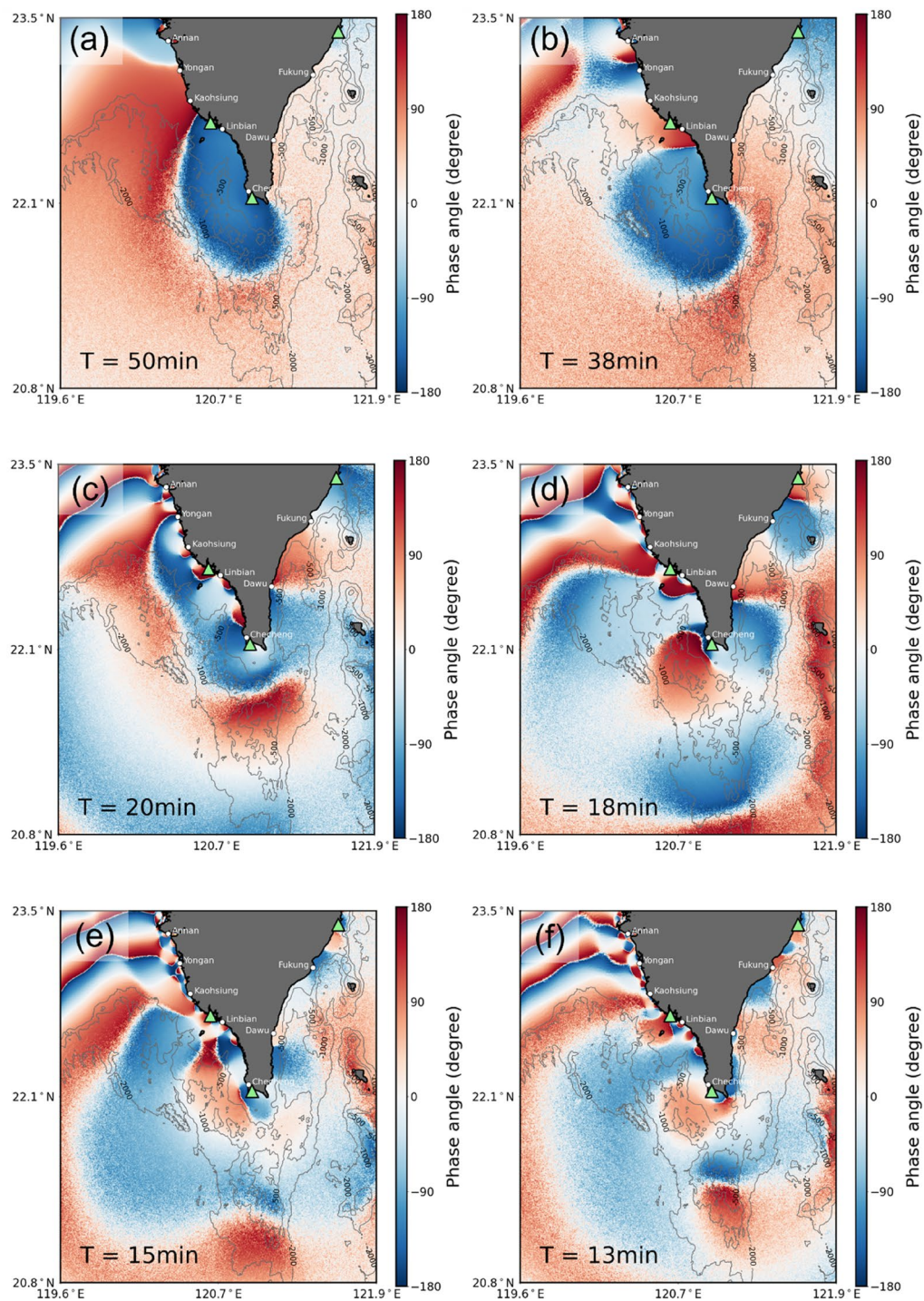


Fig. 7 Phase angles of resonant oscillation modes in the region of interest (grid-2) from the 2006 Pingtung earthquakes. Green triangles represent tide gauges. White circles indicate the coastal site locations. The bathymetry contours are represented by black solid lines

doublet, is exhibited. Fourier analyses were applied to modeled and observed time series at individual tide gauges to obtain the stationary spectral peaks for the 2006 Pingtung tsunami event. Spatiotemporal analyses

were performed on the process time series of the simulated tsunami wavefield in the region of southern Taiwan to calculate the spatially integrated spectra. The peaks of the spatially integrated spectra were compared

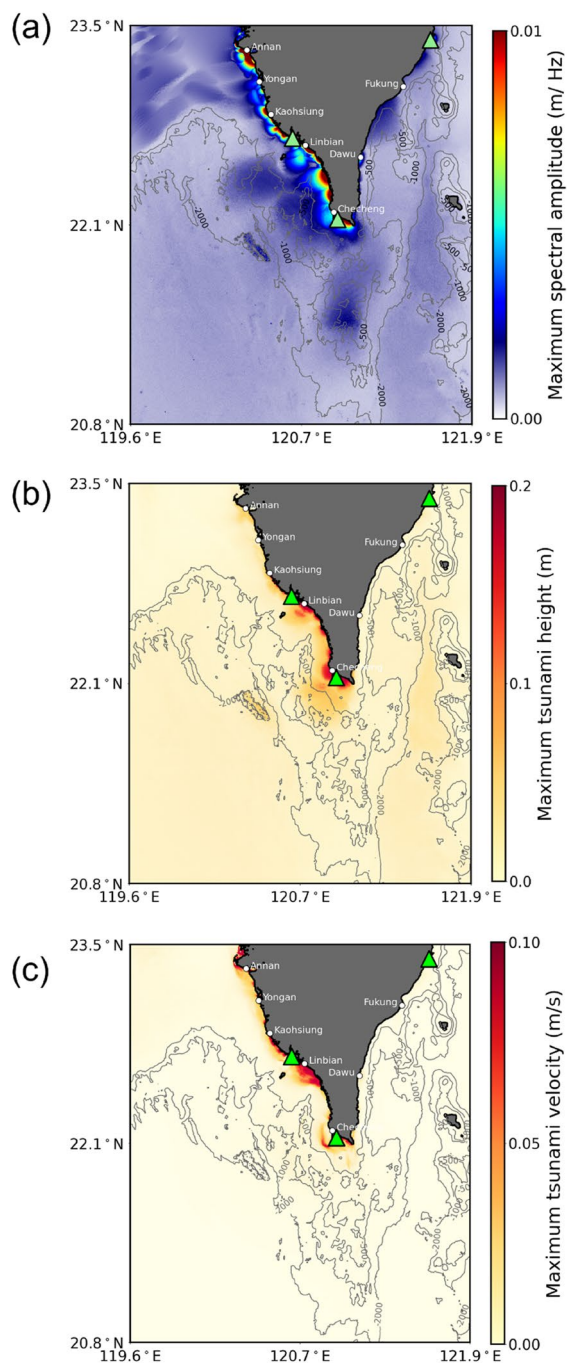


Fig. 8 Maximum **a** spectral amplitude of tsunami resonance, **b** simulated tsunami heights, and **c** simulated tsunami current velocity in grid-2 from the 2006 Pingtung earthquake. Green triangles represent tide gauges. White circles indicate the coastal site locations. The bathymetry contours are represented by black solid lines

to stationary spectral peaks to identify the main oscillation modes of the 2006 Pingtung tsunami event. The results suggested that the main oscillation modes of the 2006 tsunami were at periods of 13, 15, 18, 20, 38, and 50 min. The main oscillation periods of 13, 15, 18, and 20 min are attributed to the tsunami source periods, whereas 38 and 50 min are likely affected by the local bathymetry.

The tsunami resonance analyses were conducted based on the identified main oscillation modes of the 2006 Pingtung tsunami event. In the 2006 Pingtung tsunami, high-energy tsunami waves generally occurred along the west coast of southern Taiwan in most modes. Only the oscillation at a period of 18 min showed antinodes with energy amplification along the east coast. The propagation of the tsunami oscillation was prevented by the Hengchun Peninsula. This finding is attributed to the trapping of radiated tsunami energy over the continental shelf that extended in front of the west coast. Furthermore, the migration of the spectral amplitude distribution across the period domain also revealed that the energy amplification is a frequency-dependent coastal behavior and is responsible for the large tsunami heights and strong tsunami-induced current velocities.

This work demonstrated the resonance characteristics and impacts of nearfield tsunamis in southern Taiwan caused by the 2006 Pingtung earthquake doublet; however, various sources of far-field tsunamis should also be included and investigated in future work. The findings of this study together with earlier studies enable coastal communities in tsunamigenic areas, such as southern Taiwan, to better interpret tsunami hazards for coastal planning and emergency management for a future tsunami.

Acknowledgements

The authors would like to thank the Central Weather Bureau, R.O.C. (Republic of China) for providing the tide gauge observation data for the period of the 2006 Pingtung earthquake tsunami. The authors also thank AJE (<https://www.aje.com/>) for English language editing. Special thanks go to Mr. Kang-Jun Liu, Tohoku University, Japan, for his valuable suggestions on this work. Great thanks also go to Editor-in-Chief (Prof. Kenji Satake) and three anonymous reviewers for review comments and suggestions.

Author contributions

FI and AS supervised the research and revised the manuscript. KP provided technical support for the numerical tsunami simulation. A-CC prepared the research concept, collected the data, performed the numerical tsunami simulation, analyzed the results, and wrote the manuscript. All authors read and approved the final manuscript.

Funding

This research was partly funded by the WISE program for sustainability in the Dynamic Earth department, Tohoku University, Japan.

Availability of data and materials

The bathymetric data employed for numerical tsunami simulation was obtained from GEBCO (<https://www.gebco.net/>). The tide gauge records were supplied by Central Weather Bureau (CWB), R.O.C.

Declarations

Competing interests

All authors declare that there are no competing interests.

Received: 13 December 2022 Accepted: 8 March 2023

Published online: 14 March 2023

References

- Abe K (2009) Excitation of resonant modes along the Japanese coast by the 1993 and 1983 tsunamis in the Japan Sea. In: Pure and applied geophysics, pp 117–130
- Adriano B, Fujii Y, Koshimura S (2018) Tsunami source and inundation features around Sendai Coast, Japan, due to the November 22, 2016 M_w 6.9 Fukushima earthquake. *Geosci Lett* 5:1
- Aida I (1978) Reliability of a tsunami source model derived from fault parameters. *J Phys Earth* 26:57–73
- Aránguiz R (2015) Tsunami resonance in the bay of Concepción (Chile) and the effect of future events. *Handb Coastal Disaster Mitigation Eng Plan*. <https://doi.org/10.1016/B978-0-12-801060-0.00006-X>
- Borrero JC, Lynett PJ, Kalligeris N (2015) Tsunami currents in ports. *Philos Trans R Soc A Math Phys Eng Sci* 373:1
- Catalán PA, Aránguiz R, González G et al (2015) The 1 April 2014 Pisagua tsunami: Observations and modeling. *Geophys Res Lett* 42:2918–2925. <https://doi.org/10.1002/2015GL063333>
- Cheng SN, Shaw CF, Yeh YT (2016) Reconstructing the 1867 Keelung earthquake and Tsunami based on historical documents. *Terrest Atmos Ocean Sci* 27:431–449
- Cheng A-C, Suppasri A, Pakoksung K, Imamura F (2023) Characteristics of consecutive tsunamis and resulting tsunami behaviors in southern Taiwan induced by the Hengchun earthquake doublet on 26 December 2006. *Nat Hazard* 23:447–479. <https://doi.org/10.5194/nhess-23-447-2023>
- Cortés P, Catalán PA, Aránguiz R, Bellotti G (2017) Tsunami and shelf resonance on the northern Chile coast. *J Geophys Res Oceans* 122:7364–7379. <https://doi.org/10.1002/2017JC012922>
- Goto C, Ogawa Y, Shuto N, Imamura F (1997) Numerical method of tsunami simulation with the leap-frog scheme. *IOC Manuals Guides* 35:1–126
- Harris CR, Millman KJ, van der Walt SJ et al (2020) Array programming with NumPy. *Nature* 585:357–362
- Heidarzadeh M, Mulia IE (2021) Ultra-long period and small-amplitude tsunami generated following the July 2020 Alaska M_w 7.8 tsunamigenic earthquake. *Ocean Eng*. <https://doi.org/10.1016/j.oceaneng.2021.109243>
- Heidarzadeh M, Satake K (2013) Waveform and spectral analyses of the 2011 Japan Tsunami records on tide gauge and DART stations across the Pacific Ocean. *Pure Appl Geophys* 170:1275–1293. <https://doi.org/10.1007/s00024-012-0558-5>
- Heidarzadeh M, Satake K (2017) Possible dual earthquake-landslide source of the 13 November 2016 Kaikoura, New Zealand Tsunami. *Pure Appl Geophys* 174:3737–3749. <https://doi.org/10.1007/s00024-017-1637-4>
- Heidarzadeh M, Satake K, Murotani S et al (2015) Deep-water characteristics of the trans-Pacific Tsunami from the 1 April 2014 M_w 8.2 Iquique, Chile Earthquake. *Pure Appl Geophys* 172:719–730. <https://doi.org/10.1007/s00024-014-0983-8>
- Heidarzadeh M, Harada T, Satake K et al (2017) Tsunamis from strike-slip earthquakes in the Wharton Basin, northeast Indian Ocean: March 2016 M_w 7.8 event and its relationship with the April 2012 M_w 8.6 event. *Geophys J Int* 211:1601–1612. <https://doi.org/10.1093/gji/ggx395>
- Heidarzadeh M, Pranantyo IR, Okuwaki R et al (2021) Long tsunami oscillations following the 30 October 2020 M_w 7.0 Aegean sea earthquake: observations and modelling. *Pure Appl Geophys* 178:1531–1548. <https://doi.org/10.1007/s00024-021-02761-8>
- Heidarzadeh M, Gusman AR, Ishibe T et al (2022) Estimating the eruption-induced water displacement source of the 15 January 2022 Tonga volcanic tsunami from tsunami spectra and numerical modelling. *Ocean Eng*. <https://doi.org/10.1016/j.oceaneng.2022.112165>
- Hsu YJ, Yu SB, Simons M et al (2009) Interseismic crustal deformation in the Taiwan plate boundary zone revealed by GPS observations, seismicity, and earthquake focal mechanisms. *Tectonophysics* 479:4–18. <https://doi.org/10.1016/j.tecto.2008.11.016>
- Hsu YJ, Ando M, Yu SB, Simons M (2012) The potential for a great earthquake along the southernmost Ryukyu subduction zone. *Geophys Res Lett*. <https://doi.org/10.1029/2012GL052764>
- Imamura F, Yoshida I, Moore A (2001) Numerical study of the 1771 Meiwa tsunami at Ishigaki Island, Okinawa and the movement of the tsunami stones. *Proc Coastal Eng JSCE* 48:346–350
- Imamura F (1996) Review of Tsunami simulation with a finite difference method. *Long-wave Run-up Models* 1996:25–42
- Koshimura S (2002) Multiple reflection of tsunami incident on a continental slope. *J JSCE* 59:151–160
- Koshimura S, Imamura F, Shuto N (1996) Numerical analysis of tsunami propagates as boundary wave. *J JSCE, B2 (Coast Eng)* 1996:276–280
- Koyano K, Takabatake T, Esteban M, Shibayama T (2021) Influence of edge waves on tsunami characteristics along Kujukuri Beach, Japan. *J Waterw Port Coast Ocean Eng* 147:04020049. [https://doi.org/10.1061/\(ASCE\)WW.1943-5460.0000617](https://doi.org/10.1061/(ASCE)WW.1943-5460.0000617)
- Loomis HG (1966) Spectral analysis of tsunami records from stations in the Hawaiian islands. *Bull Seismol Soc Am* 56:697–713
- Melgar D, Ruiz-Angulo A (2018) Long-lived tsunami edge waves and shelf resonance from the M8.2 Tehuantepec earthquake. *Geophys Res Lett* 45:12414–12421. <https://doi.org/10.1029/2018GL080823>
- Miyazawa K, Goto K, Imamura F (2012) Re-evaluation of the 1771 meiwa tsunami source model, Southern Ryukyu Islands, Japan. In: Submarine mass movements and their consequences—5th international symposium. Kluwer Academic Publishers, New York, pp 497–506
- Muhari A, Charvet I, Suyoshi F et al (2015) Assessment of tsunami hazards in ports and their impact on marine vessels derived from tsunami models and the observed damage data. *Nat Hazards* 78:1309–1328. <https://doi.org/10.1007/s11069-015-1772-0>
- Munger S, Cheung KF (2008) Resonance in Hawaii waters from the 2006 Kuril Islands Tsunami. *Geophys Res Lett*. <https://doi.org/10.1029/2007GL032843>
- Nakamura M (2009) Fault model of the 1771 Yaeyama earthquake along the Ryukyu Trench estimated from the devastating tsunami. *Geophys Res Lett*. <https://doi.org/10.1029/2009GL039730>
- Okada Y (1985) Surface deformation due to shear and tensile faults in a half-space. *Carrollrhoda Books*, New York
- Okinawa Prefectural Government (2015) Okinawa Tsunami inundation assumption (in Japanese)
- Otake T, Chua CT, Suppasri A, Imamura F (2020) Justification of possible casualty-reduction countermeasures based on global tsunami hazard assessment for tsunami-prone regions over the past 400 years. *J Disaster Res* 15:490–502. <https://doi.org/10.20965/jdr.2020.p0490>
- Ren Z, Hou J, Wang P, Wang Y (2021) Tsunami resonance and standing waves in Hangzhou Bay. *Phys Fluids*. <https://doi.org/10.1063/5.0059383>
- Ren Z, Liu H, Jimenez C, Wang Y (2022) Tsunami resonance and standing waves in the South China Sea. *Ocean Eng*. <https://doi.org/10.1016/j.oceaneng.2022.112323>
- Roeber V, Yamazaki Y, Cheung KF (2010) Resonance and impact of the 2009 Samoa tsunami around Tutuila, American Samoa. *Geophys Res Lett*. <https://doi.org/10.1029/2010GL044419>
- Sheehan AF, Gusman AR, Heidarzadeh M, Satake K (2015) Array observations of the 2012 haida gwaii tsunami using cascadia initiative absolute and differential seafloor pressure gauges. *Seismol Res Lett* 86:1278–1286. <https://doi.org/10.1785/0220150108>
- Sugawara D, Yu NT, Yen JY (2019) Estimating a tsunami source by sediment transport modeling: a primary attempt on a historical/1867 normal-faulting tsunami in Northern Taiwan. *J Geophys Res Earth Surf* 124:1675–1700. <https://doi.org/10.1029/2018JF004831>

- Sun YS, Chen PF, Chen CC et al (2018) Assessment of the peak tsunami amplitude associated with a large earthquake occurring along the southernmost Ryukyu subduction zone in the region of Taiwan. *Nat Hazard* 18:2081–2092. <https://doi.org/10.5194/nhess-18-2081-2018>
- Suppasri A, Leelawat N, Latcharote P et al (2017) The 2016 Fukushima earthquake and tsunami: local tsunami behavior and recommendations for tsunami disaster risk reduction. *Int J Disaster Risk Reduct* 21:323–330. <https://doi.org/10.1016/j.ijdrr.2016.12.016>
- Suppasri A, Fukui K, Yamashita K et al (2018) Developing fragility functions for aquaculture rafts and eelgrass in the case of the 2011 Great East Japan tsunami. *Nat Hazard* 18:145–155. <https://doi.org/10.5194/nhess-18-145-2018>
- Suppasri A, Muhari A, Futami T et al (2014) Loss functions for small marine vessels based on survey data and numerical simulation of the 2011 great East Japan Tsunami. *J Waterw Port Coast Ocean Eng*. [https://doi.org/10.1061/\(asce\)www.1943-5460.0000244](https://doi.org/10.1061/(asce)www.1943-5460.0000244)
- Tanioka Y, Shibata M, Yamanaka Y et al (2019) Generation mechanism of large later phases of the 2011 Tohoku-oki tsunami causing damages in Hakodate, Hokkaido, Japan. *Prog Earth Planet Sci*. <https://doi.org/10.1186/s40645-019-0278-x>
- Tanioka Y, Satake K (1996) Tsunami generation by horizontal displacement of ocean bottom. *Geophys Res Lett* 23:861–864. <https://doi.org/10.1029/96GL00736>
- Wang Y, Zamora N, Quiroz M et al (2021) Tsunami resonance characterization in Japan Due to Trans-Pacific Sources: Response on the Bay and Continental Shelf. *J Geophys Res Oceans*. <https://doi.org/10.1029/2020JC017037>
- Wang Y, Heidarzadeh M, Satake K, Hu G (2022a) Characteristics of two tsunamis generated by successive M_w 7.4 and M_w 8.1 earthquakes in the Kermadec Islands on 4 March 2021. *Nat Hazard* 22:1073–1082. <https://doi.org/10.5194/nhess-22-1073-2022>
- Wang Y, Su HY, Ren Z, Ma Y (2022b) Source properties and resonance characteristics of the tsunami generated by the 2021 M 8.2 Alaska earthquake. *J Geophys Res Oceans*. <https://doi.org/10.1029/2021JC018308>
- Wu TR, Chen PF, Tsai WT, Chen GY (2008) Numerical study on tsunamis excited by 2006 Pingtung earthquake doublet. *Terrest Atmos Oceanic Sci* 19:705–715. [https://doi.org/10.3319/TAO.2008.19.6.705\(PT\)](https://doi.org/10.3319/TAO.2008.19.6.705(PT))
- Yamanaka Y, Nakamura M (2020) Frequency-dependent amplification of the Sanriku tsunamis in Ryori Bay. *Earth Planets Space*. <https://doi.org/10.1186/s40623-019-1128-1>
- Yamazaki Y, Cheung KF (2011) Shelf resonance and impact of near-field tsunami generated by the 2010 Chile earthquake. *Geophys Res Lett*. <https://doi.org/10.1029/2011GL047508>

Publisher's Note

Springer Nature remains neutral with regard to jurisdictional claims in published maps and institutional affiliations.

Submit your manuscript to a SpringerOpen[®] journal and benefit from:

- Convenient online submission
- Rigorous peer review
- Open access: articles freely available online
- High visibility within the field
- Retaining the copyright to your article

Submit your next manuscript at ► [springeropen.com](https://www.springeropen.com)